Observation of Landau levels and chiral edge states in photonic crystals through pseudomagnetic fields induced by synthetic strain

Barczyk, René; Kuipers, L.; Verhagen, Ewold

DOI
10.1038/s41566-024-01412-3

Publication date
2024

Document Version
Final published version

Published in
Nature Photonics

Citation (APA)
Barczyk, R., Kuipers, L., & Verhagen, E. (2024). Observation of Landau levels and chiral edge states in photonic crystals through pseudomagnetic fields induced by synthetic strain. *Nature Photonics*, *18*(6), 574-579. https://doi.org/10.1038/s41566-024-01412-3

nature photonics

Article

https://doi.org/10.1038/s41566-024-01412-3

Observation of Landau levels and chiral edge states in photonic crystals through pseudomagnetic fields induced by synthetic strain

Received: 5 June 2023

Accepted: 22 February 2024

René Barczyk[1], L. Kuipers[2] & Ewold Verhagen[1]

Control over light propagation and localization in photonic crystals offers wide applications ranging from sensing and on-chip routing to lasing and quantum light–matter interfaces. Although in electronic crystals, magnetic fields can be used to induce a multitude of unique phenomena, the uncharged nature of photons necessitates alternative approaches to bring about similar control over photons at the nanoscale. Here we experimentally realize pseudomagnetic fields in two-dimensional photonic crystals through engineered strain of the lattice. Analogous to strained graphene, this induces flat-band Landau levels at discrete energies. We study the spatial and spectral properties of these states in silicon photonic crystals at telecom wavelengths with far-field spectroscopy. Moreover, taking advantage of the photonic crystal's design freedom, we realize domains of opposite pseudomagnetic field and observe chiral edge states at their interface. We reveal that the strain-induced states can achieve remarkably high quality factors despite being phase matched to the radiation continuum. Together with the high density of states and high degeneracy associated with flat bands, this provides powerful prospects for enhancing light–matter interactions, and illustrates the broad potential of psdeudomagnetic fields in the nanophotonic domain. This work, thus, establishes a new design principle to govern both on-chip and radiating light fields.

In condensed-matter physics, magnetic fields provide a versatile mechanism to control the behaviour of electrons in materials. For example, a magnetic field piercing a two-dimensional electron gas induces flat bands at discrete energies known as Landau levels, which can be viewed as the quantization of the electrons' cyclotron motion in the magnetic field. Moreover, at the system's boundaries, the magnetic field implies the existence of chiral edge states associated with the quantum Hall effect. In photonics, the idea of controlling light in a similar way has been a tantalizing prospect. Although at microwave frequencies, magneto-optic effects may be strong enough to effectively mediate interactions between photons and real magnetic fields[1], this approach is unfeasible for optical frequencies. Realizing an effective magnetic control over photons in dielectric photonic systems without relying on actual external magnetic fields represents an especially luring proposition for on-chip nanophotonic systems, where the associated implications for the localization and steering of light and the enhancement of light–matter interactions form powerful prospects.

---

[1]Center for Nanophotonics, AMOLF, Amsterdam, The Netherlands. [2]Kavli Institute of Nanoscience, Delft University of Technology, Delft, The Netherlands.
e-mail: verhagen@amolf.nl

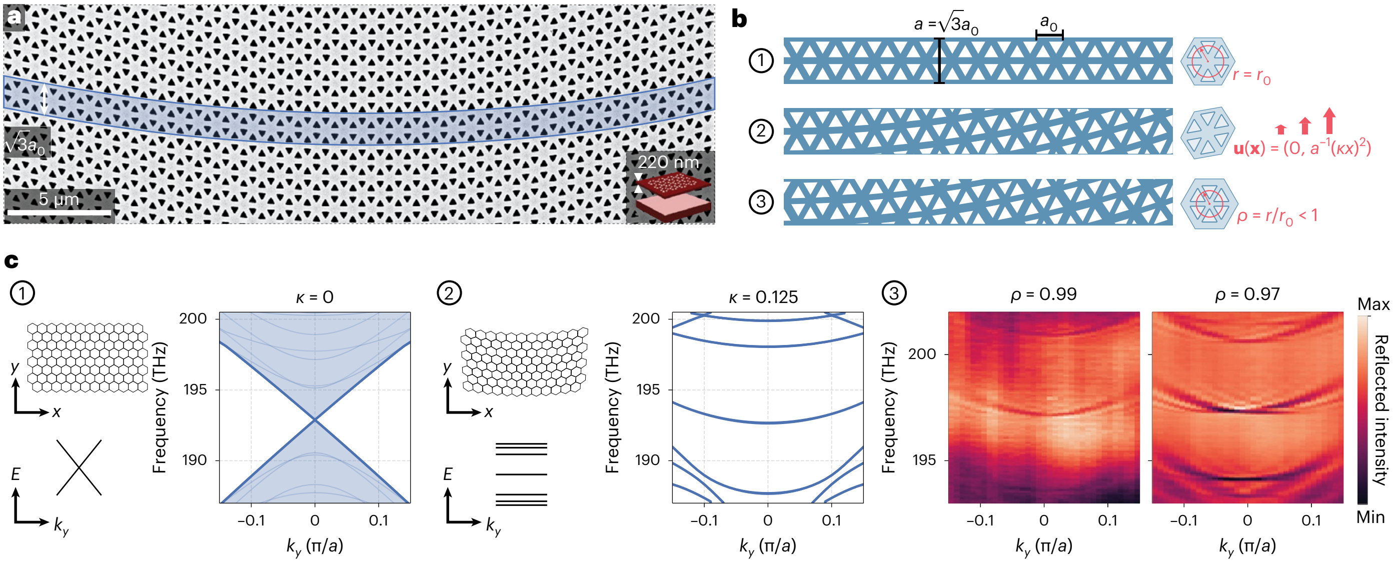

Fig. 1 | Sample geometry and strain-induced Landau levels. a, Scanning electron micrograph of a fabricated PhC membrane, with the sample geometry depicted in the inset. The supercell of the strained honeycomb lattice is highlighted in blue, with periodicity $a = \sqrt{3}a_0$ along the *y* direction and a_0 denoting the lattice constant of the underlying pristine honeycomb lattice. **b**, Schematic of the supercells for pristine ①, strained ② and shrunken strained ③ lattices. The applied displacement function is given by $\mathbf{u}(\mathbf{x})$, and $\rho = r/r_0$ denotes the relative displacement of holes within a hexagonal unit cell with respect to a pristine lattice ($\rho = 1$). **c**, Schematic of the real-space geometry and dispersion of a pristine honeycomb lattice (left), together with simulated photonic bulk bands ①. The dispersion is characterized by a Dirac-type linear crossing. Because of the two-dimensional periodicity of the lattice, the dispersion delineates a continuum of states in the Dirac cone (indicated by blue shading). The light-blue lines depict bands of an exemplary finite-width supercell with transverse periodic boundary conditions at $x = \pm 28.5a_0$. A bandgap is opened in place of the original Dirac-type crossing due to strain ②, and flat Landau levels emerge symmetrically distributed around the bandgap centre. Experimentally retrieved angularly resolved reflection spectra showing photonic Landau levels in strained PhC lattices ③, with $\rho = 0.99$ and 0.97 and $\kappa = 0.125$ in both cases.

In graphene, pseudomagnetic fields (PMFs) can be induced for electrons via mechanical strain of the lattice, as the corresponding perturbation to interatomic hopping mimics the action of a magnetic gauge potential[2–5]. Contrary to real magnetic fields that break time-reversal symmetry, strain-induced PMFs carry opposite signs for the two non-equivalent Dirac cones at the K and K′ valleys. Nevertheless, they still give rise to intriguing phenomena including Landau-level quantization and chiral edge states. Analogously, suitable lattice deformations can act as magnetic gauge potentials in bosonic systems. Their effects have been studied in lattices of coupled waveguides[6,7], arrays of microwave resonators[8,9], Moiré superlattices in bilayer microwave metamaterials[10], microcavity exciton–polaritons[11] and acoustic platforms[12–16]. Recently, it has been predicted that inhomogeneous deformations in honeycomb photonic crystal (PhC) membranes can act as a magnetic gauge potential, creating synthetic strain through a designed perturbation of the dielectric function $\epsilon(\mathbf{x})$ (ref. 17). Strain-induced pseudomagnetism in PhCs is non-trivial because of inherent long-range interactions. It would, however, be highly appealing as it provides a new paradigm for the on-chip routing and confinement of light[18,19]. In contrast to Landau levels in cavity or waveguide arrays[6,11,20] or multimode cavities[21], their realization in nanophotonics via PMFs offers a path to enhance light–matter interactions and nonlinearities through the high degeneracy and high local density of states of photonic Landau levels, associated with their nature as flat bands[22–25]. Moreover, photonic synthetic magnetism has been predicted to enable unique forms of lasing[26], polariton condensation[27] and optical vortex generation[28], and could form a new design paradigm in metamaterials to control far-field radiation.

Here we realize PMFs in silicon PhCs at telecom wavelengths, and demonstrate the resulting emergence of photonic Landau levels. Using far-field Fourier spectropolarimetry[29–31], we study the characteristic energy scaling of Landau levels with strain, their delocalization and loss mechanisms. We reveal that they can exhibit remarkably high quality factors, even though they exist within the radiation continuum. We finally demonstrate the creation of inhomogeneous PMFs by spatially tailoring the strain field. This allows observing signatures of chiral edge states that are predicted to exist at the boundaries of domains with opposite magnetic fields[32] and which are distinct from other crystal-symmetry-based implementations of topological edge states in PhCs[19,33–35]. Our findings illustrate the applicability of synthetic strain engineering for the control of light and its interaction with matter at the nanoscale.

Results

Observation of nanophotonic Landau levels

We fabricate suspended silicon membranes perforated by triangular air holes using electron-beam lithography and wet etching of a silicon-on-insulator substrate (Methods)[36,37]. Figure 1a shows a scanning electron micrograph of a fabricated strained PhC lattice, where the inset depicts a three-dimensional cross-cut of the slab. We follow the approach outlined elsewhere[17] to induce a uniform PMF $\mathbf{B}_{\text{eff}}$ piercing the PhC plane. The starting point is a pristine transverse-electric-type honeycomb PhC with lattice constant a_0 and dielectric distribution $\epsilon(\mathbf{x})$ ($\mathbf{x} = (x, y)$). The lattice is oriented with the zigzag and armchair directions along the *x* and *y* axes, respectively. The PhC's frequency spectrum features a Dirac-type crossing (Fig. 1b,c) and is governed by the scalar Helmholtz equation for the out-of-plane magnetic field $\mathbf{H}(\mathbf{x}) = H_z(\mathbf{x})\hat{\mathbf{z}}$:

$$-\nabla \cdot (\epsilon^{-1}(\mathbf{x})\nabla)H_z(\mathbf{x}) = (\omega/c)^2 H_z(\mathbf{x}). \quad (1)$$

Figure 1c plots the calculated dispersion for the k_y direction, with the Dirac point appearing at $k_y = 0$ for lattice constant $a = \sqrt{3}a_0$, which is the minimal periodicity when implementing the strain profile. This uniaxial strain is realized by displacing each point $\mathbf{x}$ in the PhC plane via $T(\mathbf{x}) = \mathbf{x} + \mathbf{u}(\mathbf{x})$, with quadratic displacement function

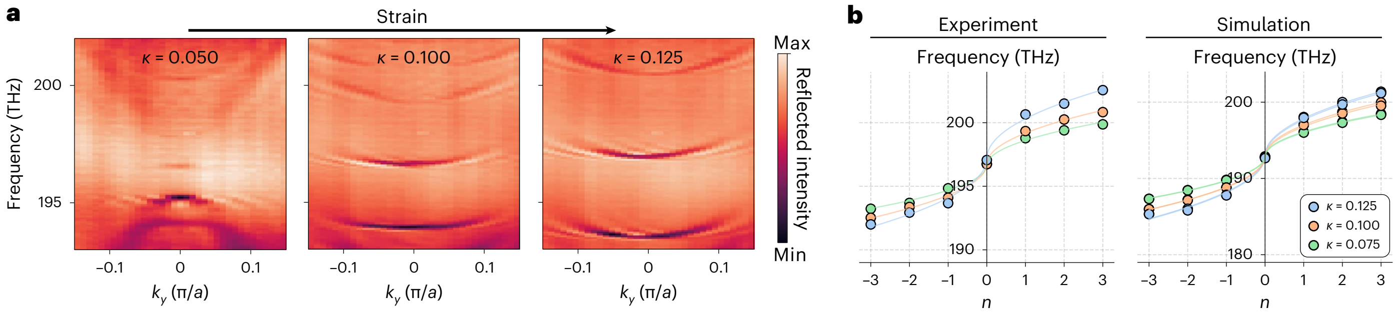

Fig. 2 | Photonic Landau levels in increasingly strong PMFs. a, Far-field reflection spectra displaying the evolution of photonic bands with increasing strain magnitude κ. **b**, Experimentally and numerically extracted centre-mode frequencies of photonic Landau levels for varying κ values, fitted with a square-root scaling law. The small mode splitting of the (ideally doubly degenerate) modes in simulations is a finite-size effect and not resolvable in our far-field measurements.

$\mathbf{u}(\mathbf{x}) = (0, a^{-1}(\kappa x)^2)$ and the parameter κ representing the strain magnitude. The displacement, thus, breaks the x periodicity but preserves the larger supercell periodicity a along y. In the vicinity of the K and K′ valleys, the eigenfunctions' dynamics are captured by a two-dimensional Dirac-type Hamiltonian[3]:

$$H_{\text{eff}} = v_{\text{D}}[-\mathrm{i}\nabla_{\mathbf{x}} - \mathbf{A}_{\text{eff}}(\mathbf{x})]\cdot\sigma, \qquad (2)$$

where v_{D} is the Dirac velocity, $\sigma = (\sigma_1, \sigma_2)$ are Pauli matrices and $\mathbf{A}_{\text{eff}}$ is the effective magnetic vector potential that is related to the displacement function $\mathbf{u}$ via

$$\mathbf{A}_{\text{eff}} \propto \begin{pmatrix} u_{x,x} - u_{y,y} \\ -(u_{x,y} + u_{y,x}) \end{pmatrix}. \qquad (3)$$

Here $u_{i,j} = \partial u_i/\partial x_j$. The solutions to the eigenvalue problem associated with equation (2), up to first-order $\mathcal{O}(\kappa)$, correspond to flat states at discrete frequencies that are symmetrically distributed around the original Dirac-cone frequency ω_{D}. These constitute Landau levels that follow the square-root law:

$$\omega_n = \omega_{\text{D}} \pm \frac{v_{\text{D}} c^2}{\sqrt{2\omega_{\text{D}}}}\sqrt{n|\mathbf{B}_{\text{eff}}(\kappa)|}, \quad n = 0, 1, 2, \ldots, \qquad (4)$$

where the effective magnetic-field amplitude is given by $|\mathbf{B}_{\text{eff}}(\kappa)| = |\nabla_{\mathbf{x}} \times \mathbf{A}_{\text{eff}}(\kappa)| = B_0\kappa^2$, and B_0 is a constant parameter specific to the (meta) material[17,32]. Although this magnetic field does not quantize conductance, given that photons obey bosonic rather than fermionic statistics, it does quantize the spectrum.

To make the strain-induced photonic Landau levels experimentally accessible via far-field Fourier spectroscopy (Extended Data Fig. 1 and Methods), we enhance their radiative coupling by applying an additional type of sub-lattice symmetry breaking by concentrically shrinking the radial position r of six air holes within a hexagonal unit cell by a factor of $\rho = r/r_0$ (Fig. 1b,c), where $r = r_0$ for the pristine honeycomb PhC[29–31,33]. Figure 1c presents the wavevector- and frequency-resolved reflectance for two shrinking factors, namely, $\rho = 0.99$ and 0.97, highlighting the substantial enhancement in band visibility achieved through the symmetry-breaking mechanism. Here we recognize pronounced, largely horizontal bands in the photonic dispersion, in a striking departure from the linear Dirac-cone dispersion of the unperturbed lattice. This constitutes the first pivotal consequence of the PMFs we realized—the experimental observation of photonic Landau levels in a strained PhC membrane. The clarity with which these states can be resolved is testament to the low loss and large scale of the PhC implementation. The Landau levels are unaffected by the shrinking factor (Extended Data Fig. 2 shows more measurements and simulations with varying ρ values). They are distributed around the $n = 0$ Landau level at $\omega_{\text{D}} \approx 2\pi \times 197$ THz and exhibit Fano lineshapes due to interference with the broad reflection background (Methods). In the following, if not stated otherwise, the presented reflection measurements are of PhCs with $\rho = 0.98$ that have bands that are well visible as weak symmetry breaking is maintained. We emphasize that the symmetry breaking is only used here to visualize the states. Alternative methods such as period doubling could also be employed, whereas perturbations that break inversion symmetry are to be avoided to not affect the Landau levels.

The strain magnitude, controlled by the parameter κ, largely affects the energy landscape of the PhC (Fig. 2a; Extended Data Fig. 3 shows more measurements and simulations with varying κ values). We see that the bandgap size increases with κ, and successively more flat states emerge around ω_{D}. Extracting their centre-mode frequencies at the Γ point from fits to the experimental lineshape (equation (5)), we recognize that the level separation follows the expected square-root scaling that is unique to massless Dirac particles in an increasingly strong external (pseudo-)magnetic field (equation (4)). This characteristic energy scaling is further supported by eigenfrequency simulations (Fig. 2b). Together, the results shown in Fig. 2 underline the origin of the resolved states in the strain-induced PMF.

Localization and radiation

Long-range interactions in the PhC lattice render the photonic Landau levels weakly dispersive away from the Γ point, increasing in frequency with $|k_y|$ (Fig. 2a)[17]. Coupling beyond next-nearest neighbours corresponds to higher-order contributions ($\mathcal{O}(\kappa^2)$) in equation (4). It, thus, represents a feature specific to the photonic platform, differentiating it from the tight-binding graphene analogue. The spatial localization of states also displays a clear dependence on k_y. Figure 3a shows the simulated fields of the $n = 0$ Landau level at three different k_y values. All the bands are doubly degenerate, with fields that are even and odd with respect to the mirror symmetry axis of the lattice along $x = 0$—or an orthogonal pair of superpositions thereof (Fig. 3a, right). Although the states' transverse extent for $k_y = 0$—where the group velocity vanishes—spans many unit cells, it appears finite nonetheless. For a finite wavevector k_y, the fields are localized further away from the centre, eventually transforming into trivial states propagating along the armchair edges of the lattice (Fig. 3a)[17,38,39]. We see this behaviour confirmed in experiment when scanning the excitation focus along x (Fig. 3b). Here we plot the measured states for two specific incident polarizations (right- and left-handed circularly polarized; Extended Data Fig. 4 shows the case of linear polarization). Interestingly, we recognize that a mode with positive k_y can be excited either with right-circular polarization to the left of the centre ($x = -3$ μm) or with left-circular polarization to the right ($x = 3$ μm). Thus, these states form a degenerate pair with opposite pseudospins (encoded as far-field helicity) linked to transverse localization. We note that an equivalent pair with opposite handedness exists in the backward

https://doi.org/10.1038/s41566-024-01412-3

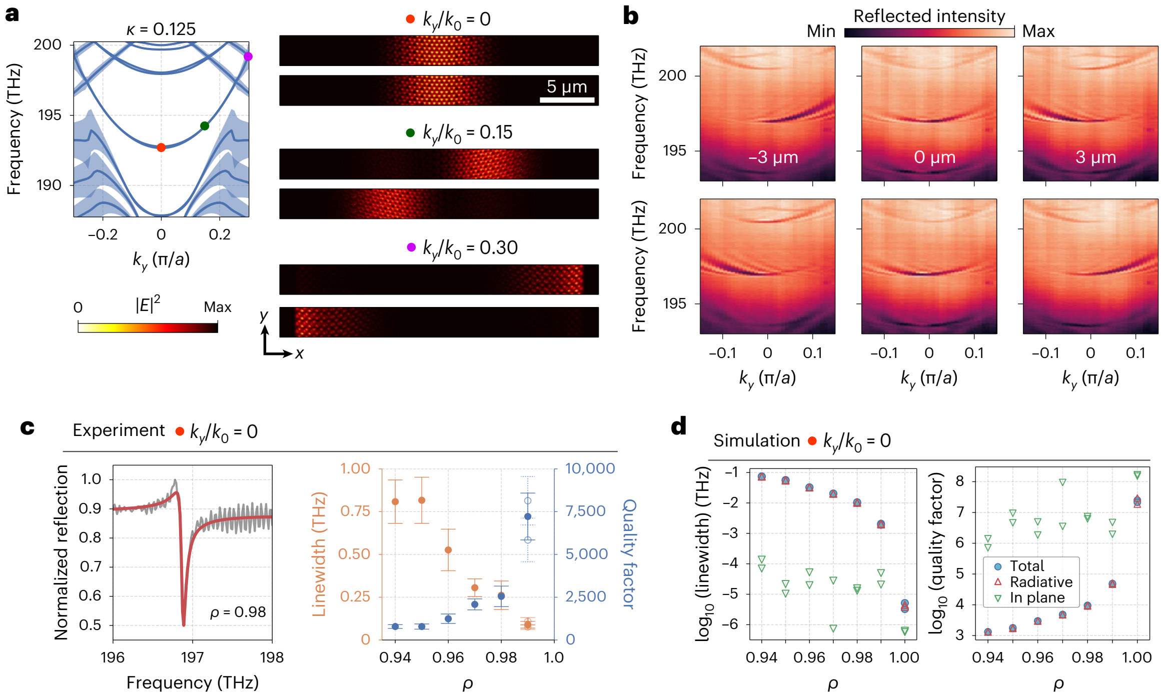

Fig. 3 | Landau-level localization, polarization and losses. a, Simulated bands of a strained lattice ($\kappa = 0.125, \rho = 0.98$) with the linewidth indicated by blue shading (left), alongside the simulated mode profiles of the in-plane electric-field intensity for selected values of k_y (right). **b**, Position- and polarization-dependent excitation of photonic Landau levels, where the displacement in x relative to the lattice centre and the right-hand (R) and left-hand (L) polarization states of the incident beam are indicated. **c**, Fano fits to the measured lineshapes (left) yield the experimentally extracted linewidths and quality factors of the $n = 0$ Landau level at the Γ point as a function of ρ (right). For $\rho = 0.99$, the open circles indicate measurements on two additional lattices with different lattice constants. The linewidths are averaged over seven cross-cuts of the recorded dispersion along k_y (around $k_y \approx 0$) and given alongside the standard error. **d**, Numerically retrieved linewidths (left) and quality factors (right), showing the respective contributions of radiative and in-plane losses to the total mode loss.

direction, owing to time-reversal symmetry. For excitation near the centre ($x = 0$), the flat part of the band near $k_y = 0$ is probed for any polarization.

The transverse localization is also linked to the losses of the states, manifested in their resonance linewidths. We distinguish four possible sources of loss: (1) intrinsic far-field radiation, due to the fact that the states inherently reside within the radiation continuum; (2) losses associated with the edge of the lattice at large $|x|$, due to either scattering or leakage into slab modes; (3) losses due to scattering at random disorder; and (4) radiation losses associated with non-unity shrinking factor ρ, which are intentionally introduced only to facilitate free-space measurements. At the Γ point, we determine the quality factors of the $n = 0$ level from linewidth fits (Fig. 3c). The measured quality factors reach $Q \approx 7{,}000$ for the weakest symmetry breaking at $\rho = 0.99$, close to the spectral-resolution limit (Methods). These low losses are reproduced on PhCs with different lattice constants. The fact that losses increase strongly with smaller ρ shows that at $k_y = 0$, they are limited by the non-intrinsic losses due to non-unity ρ. In fact, the linearly decreasing trend of linewidth with ρ shows that losses are negligibly small when extrapolated to $\rho = 1$. Numerical simulations with and without absorbing boundary conditions (Methods) indeed show that radiative losses dominate (Fig. 3d, left), with intrinsic quality factor ($\rho = 1$) calculated to be on the order of $Q \approx 10^7$ (Fig. 3d, right, and Extended Data Fig. 5a). This is a remarkably high value, given that the photonic Landau levels are inherently residing within the free-space radiation continuum, as evident from the numerical simulations of the complex mode frequencies (Fig. 3a). Therefore, although strain perturbation strongly alters the real parts of the spectrum, transforming the linear Dirac dispersion into flat Landau levels, it leaves the imaginary parts close to zero. From the k_y-dependent reflection spectra (Fig. 3b), we see that resonance linewidths increase away from the Γ point. This can be related to the shift in localization away from the lattice centre towards the edges, accompanied by increased in-plane losses (point (2) above) that dominate for large wavevectors (Extended Data Fig. 6 shows the simulations of losses versus k_y).

Chiral edge states at domain walls

A defining advantage of the PhC platform is the ease with which optical potentials can be tailored at will as a function of position. Indeed, different gauge potentials (equation (3)) can be realized through different deformations $\mathbf{u}(\mathbf{x})$. By choosing $\mathbf{u}(\mathbf{x}) = (0, a^{-1}(\kappa x)^2 \mathrm{sgn}(x))$, that is, enforcing inversion rather than mirror symmetry in the $x = 0$ plane of the PhC, we obtain two oppositely strained domains that feature a domain wall between oppositely oriented PMFs at $x = 0$ (Fig. 4a,b). Numerical simulations predict the emergence of non-degenerate chiral edge states at the interface, connecting the former Landau levels of the individual half-domains (Fig. 4c, left)[32]. The origin of these states differs from that of topological edge states in other PhCs[33,40] as they arise not from a breaking of internal symmetry of a unit cell but rather a global change in the lattice. We choose propagation along an armchair boundary as we aim to avoid trivial zero-energy states at the outer boundaries of the sample that are known to be supported by the zigzag terminations of a graphene lattice[32].

The edge states are localized at the central boundary for $k_y/k_0 = 0$, but now feature a finite group velocity there (Fig. 4c, left). Like the Landau levels, they are largely protected from diffraction loss at the PhC terminations, resulting in similarly narrow linewidths and theoretical quality factors up to 10^6 (Extended Data Fig. 5b). Away from the Γ point, the edge states are increasingly displaced from the central domain wall and slowly restore their degeneracy and photonic Landau-level nature, before eventually turning into trivial propagating states at the PhC boundaries (Fig. 4d), accompanied by enhanced losses and broadened linewidth (Extended Data Fig. 5b).

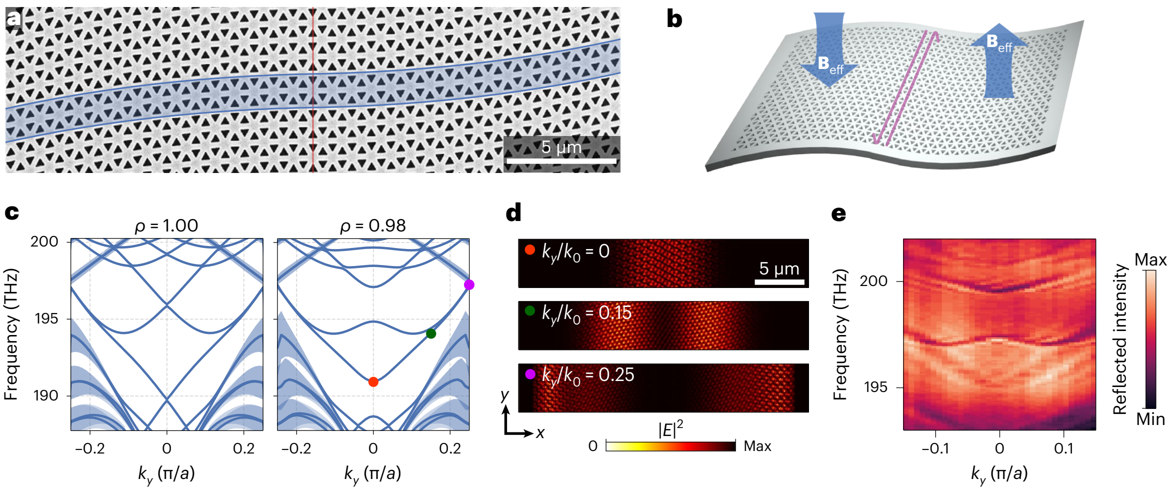

Fig. 4 | Chiral edge states through inhomogeneous PMFs. a,**b**, Scanning electron micrograph (**a**) and schematic (**b**) of a PhC membrane composed of inversely strained domains sharing an armchair interface. The opposing PMFs ($\pm\mathbf{B}_{\mathrm{eff}}$) penetrating both domains (blue arrows) lead to the emergence of counterpropagating, spin-polarized chiral edge states guided along their mutual boundary (magenta arrows). **c**, Simulated bands for the pristine ($\rho = 1.00$) and shrunken ($\rho = 0.98$) case. **d**, Real-space edge-state mode profiles of the in-plane electric-field intensity for the values of k_y marked in **c**. **e**, Edge-state spectra for a strain magnitude of $\kappa = 0.125$, taken for linear horizontal polarization with the focus spot placed 3 µm to the side of the interface.

The mode localization and associated losses can be broadly tuned by means of changing the PMF magnitude (Extended Data Fig. 7 shows the experiments and simulations with varying κ values) or by realizing more complex strain patterns. Figure 4e shows a Fourier spectroscopy measurement. The symmetry breaking at $\rho < 1$ induced to enhance radiative coupling now alters the chiral-edge-state dispersion, introducing avoided crossings at the Γ point (Fig. 4c, right; Extended Data Fig. 9 shows the data for varying ρ values). Nonetheless, much of the characteristic features of the predicted chiral edge states can be recognized in the dispersion bands, compared with the theory prediction (Fig. 4c, right). As shown in Extended Data Fig. 8, we recognize the signatures of spin–orbit coupling in the chiral edge states when resolving polarization. At a fixed frequency, one can selectively couple into forward- or backward-propagating modes by changing the helicity (pseudospin) of the incident beam. However, contrary to other implementations of edge states in PhCs based on the quantum spin Hall effect[30,33], there is no unique correspondence between the states' pseudospin and the far-field helicity of the emitted radiation, as the same state can be excited with different helicities at different locations.

Discussion

We demonstrated the experimental realization of PMFs in PhC membranes via engineered synthetic strain, and employed it to induce photonic Landau levels and quantum-Hall-like edge states in the photonic band structure. We studied these states in the far field by introducing radiative coupling through sub-lattice symmetry breaking. The latter could, however, be readily removed, leaving remarkably high quality factors despite the states being coupled to the radiation continuum. In fact, these PhC Landau levels share some traits with bound states in the continuum[41], combining low radiation coupling and spatial delocalization. Although the predicted extreme quality factors (~10^7) may not be reached in practice due to random fabrication disorder, the low loss augments the high interest of these states for applications that benefit from strong field enhancement. Together with the slow group velocity and large delocalization, it makes the flat Landau-level bands extremely appealing for a variety of applications, including quantum light sources, nonlinear nanophotonics for frequency conversion, efficient lasers, sensors, interaction of light with free electrons[25] and polariton condensation[27]. Supplementary Section II provides a preliminary numerical study showing that Purcell factors that are competitive with slow-light waveguides are in reach even without optimization, indicating high value for applications[42]. The ability to realize broad-angle resonances with ultralow intrinsic loss provides interesting prospects for wavefront control in metasurfaces, for example, for narrow-band filters and fibre couplers.

Studying the effects of disorder forms an obvious direction of follow-up research. Although we recognize that the Landau levels are unaffected by certain perturbations (such as the employed shrinking transformation), the fact that the system conserves time-reversal symmetry means that other perturbations, specifically those breaking inversion symmetry, may affect the Landau levels. This is the same in the fermionic case of strained graphene, where disorder is also a topic of interest[43]. The low-loss, large-scale silicon PhC platform forms, in fact, an interesting testbed for fundamental studies in this direction, as well as for the exploration of two-dimensional photonic Anderson localization. Likewise, it would be useful to gain a comprehensive understanding of radiative losses in these inherently non-Hermitian systems.

The demonstrated design principle of artificial strain engineering allows for a broad engineering of the localization and propagation properties of PhCs, and offers extensive control over dispersion through tailoring of the lattice, well beyond the studies reported here. For instance, the flatness of the Landau-level bands could be readily improved by engineering an effective pseudoelectric field through additional transverse strain along x when exploring applications of light–matter enhancement[17]. We numerically illustrate such flattening and the resultant increase in Purcell enhancement (Supplementary Section II). Although the optimization of a single Landau level for applications would be valuable, we note that it would be interesting to develop a comprehensive understanding of possible transformations for the complete design of dispersion. Overall, the demonstrated strain-induced gauge fields provide a new, highly flexible paradigm for the exploration of novel photonic phenomena and the potential development of new photonic devices.

Online content

Any methods, additional references, Nature Portfolio reporting summaries, source data, extended data, supplementary information, acknowledgements, peer review information; details of author contributions and competing interests; and statements of data and code availability are available at https://doi.org/10.1038/s41566-024-01412-3.

References

1. Wang, Z., Chong, Y., Joannopoulos, J. D. & Soljačić, M. Observation of unidirectional backscattering-immune topological electromagnetic states. *Nature* **461**, 772–775 (2009).
2. Kane, C. L. & Mele, E. J. Size, shape, and low energy electronic structure of carbon nanotubes. *Phys. Rev. Lett.* **78**, 1932–1935 (1997).
3. Guinea, F., Katsnelson, M. I. & Geim, A. K. Energy gaps and a zero-field quantum Hall effect in graphene by strain engineering. *Nat. Phys.* **6**, 30–33 (2010).
4. Levy, N. et al. Strain-induced pseudo–magnetic fields greater than 300 Tesla in graphene nanobubbles. *Science* **329**, 544–547 (2010).
5. Gomes, K. K., Mar, W., Ko, W., Guinea, F. & Manoharan, H. C. Designer Dirac fermions and topological phases in molecular graphene. *Nature* **483**, 306–310 (2012).
6. Rechtsman, M. C. et al. Strain-induced pseudomagnetic field and photonic Landau levels in dielectric structures. *Nat. Photon.* **7**, 153–158 (2013).
7. Song, W. et al. Dispersionless coupling among optical waveguides by artificial gauge field. *Phys. Rev. Lett.* **129**, 053901 (2022).
8. Bellec, M., Poli, C., Kuhl, U., Mortessagne, F. & Schomerus, H. Observation of supersymmetric pseudo-Landau levels in strained microwave graphene. *Light Sci. Appl.* **9**, 146 (2020).
9. Jia, H. et al. Experimental realization of chiral Landau levels in two-dimensional Dirac cone systems with inhomogeneous effective mass. *Light Sci. Appl.* **12**, 165 (2023).
10. Wang, W. et al. Moiré fringe induced gauge field in photonics. *Phys. Rev. Lett.* **125**, 203901 (2020).
11. Jamadi, O. et al. Direct observation of photonic Landau levels and helical edge states in strained honeycomb lattices. *Light Sci. Appl.* **9**, 144 (2020).
12. Duan, G. et al. Synthetic gauge fields and Landau levels in acoustic Moiré superlattices. *Appl. Phys. Lett.* **123**, 021702 (2023).
13. Wen, X. et al. Acoustic Landau quantization and quantum-Hall-like edge states. *Nat. Phys.* **15**, 352–356 (2019).
14. Yang, Z., Gao, F., Yang, Y. & Zhang, B. Strain-induced gauge field and Landau levels in acoustic structures. *Phys. Rev. Lett.* **118**, 194301 (2017).
15. Abbaszadeh, H., Souslov, A., Paulose, J., Schomerus, H. & Vitelli, V. Sonic Landau levels and synthetic gauge fields in mechanical metamaterials. *Phys. Rev. Lett.* **119**, 195502 (2017).
16. Peri, V., Serra-Garcia, M., Ilan, R. & Huber, S. D. Axial-field-induced chiral channels in an acoustic Weyl system. *Nat. Phys.* **15**, 357–361 (2019).
17. Guglielmon, J., Rechtsman, M. C. & Weinstein, M. I. Landau levels in strained two-dimensional photonic crystals. *Phys. Rev. A* **103**, 013505 (2021).
18. Salerno, G., Ozawa, T., Price, H. M. & Carusotto, I. How to directly observe Landau levels in driven-dissipative strained honeycomb lattices. *2D Mater.* **2**, 034015 (2015).
19. Salerno, G., Ozawa, T., Price, H. M. & Carusotto, I. Propagating edge states in strained honeycomb lattices. *Phys. Rev. B* **95**, 245418 (2017).
20. Hafezi, M., Demler, E. A., Lukin, M. D. & Taylor, J. M. Robust optical delay lines with topological protection. *Nat. Phys.* **7**, 907–912 (2011).
21. Schine, N., Ryou, A., Gromov, A., Sommer, A. & Simon, J. Synthetic Landau levels for photons. *Nature* **534**, 671–675 (2016).
22. Borregaard, J., Sørensen, A. S. & Lodahl, P. Quantum networks with deterministic spin–photon interfaces. *Adv. Quantum Technol.* **2**, 1800091 (2019).
23. Krauss, T. F. Why do we need slow light? *Nat. Photon.* **2**, 448–450 (2008).
24. Smirnova, D., Leykam, D., Chong, Y. & Kivshar, Y. Nonlinear topological photonics. *Appl. Phys. Rev.* **7**, 021306 (2020).
25. Yang, Y. et al. Photonic flatband resonances for free-electron radiation. *Nature* **613**, 42–47 (2023).
26. Schomerus, H. & Halpern, N. Y. Parity anomaly and Landau-level lasing in strained photonic honeycomb lattices. *Phys. Rev. Lett.* **110**, 013903 (2013).
27. Lledó, C., Carusotto, I. & Szymanska, M. Polariton condensation into vortex states in the synthetic magnetic field of a strained honeycomb lattice. *SciPost Phys.* **12**, 068 (2022).
28. Sheng, C. et al. Bound vortex light in an emulated topological defect in photonic lattices. *Light Sci. Appl.* **11**, 243 (2022).
29. Gorlach, M. A. et al. Far-field probing of leaky topological states in all-dielectric metasurfaces. *Nat. Commun.* **9**, 909 (2018).
30. Parappurath, N., Alpeggiani, F., Kuipers, L. & Verhagen, E. Direct observation of topological edge states in silicon photonic crystals: spin, dispersion, and chiral routing. *Sci. Adv.* **6**, eaaw4137 (2020).
31. Barczyk, R. et al. Interplay of leakage radiation and protection in topological photonic crystal cavities. *Laser Photonics Rev.* **2022**, 2200071 (2022).
32. Huang, Z.-T. et al. Pattern-tunable synthetic gauge fields in topological photonic graphene. *Nanophotonics* **11**, 1297–1308 (2022).
33. Wu, L.-H. & Hu, X. Scheme for achieving a topological photonic crystal by using dielectric material. *Phys. Rev. Lett.* **114**, 223901 (2015).
34. Kiriushechkina, S. et al. Spin-dependent properties of optical modes guided by adiabatic trapping potentials in photonic Dirac metasurfaces. *Nat. Nanotechnol.* **18**, 875–881 (2023).
35. Ren, B. et al. Zero-energy edge states and solitons in strained photonic graphene. *Phys. Rev. A* **107**, 043504 (2023).
36. Barik, S., Miyake, H., DeGottardi, W., Waks, E. & Hafezi, M. Two-dimensionally confined topological edge states in photonic crystals. *New J. Phys.* **18**, 113013 (2016).
37. Reardon, C. P., Rey, I. H., Welna, K., O'Faolain, L. & Krauss, T. F. Fabrication and characterization of photonic crystal slow light waveguides and cavities. *J. Vis. Exp.* e50216 (2012).
38. Akhmerov, A. R. & Beenakker, C. W. J. Boundary conditions for Dirac fermions on a terminated honeycomb lattice. *Phys. Rev. B* **77**, 085423 (2008).
39. Kohmoto, M. & Hasegawa, Y. Zero modes and edge states of the honeycomb lattice. *Phys. Rev. B* **76**, 205402 (2007).
40. Ma, T. & Shvets, G. All-Si valley-Hall photonic topological insulator. *New J. Phys.* **18**, 025012 (2016).
41. Hsu, C. W., Zhen, B., Stone, A. D., Joannopoulos, J. D. & Soljačić, M. Bound states in the continuum. *Nat. Rev. Mater.* **1**, 16048 (2016).
42. Lodahl, P., Mahmoodian, S. & Stobbe, S. Interfacing single photons and single quantum dots with photonic nanostructures. *Rev. Mod. Phys.* **87**, 347 (2015).
43. Settnes, M., Leconte, N., Barrios-Vargas, J. E., Jauho, A.-P. & Roche, S. Quantum transport in graphene in presence of strain-induced pseudo-Landau levels. *2D Mater.* **3**, 034005 (2016).

Methods

Numerical simulations

Full-wave finite-element-method simulations in three dimensions were performed using the COMSOL Multiphysics RF Module[44]. The refractive index of silicon was set to $n = 3.48$, with a slab thickness of 220 nm. The unstrained primitive rhombic unit cell consisted of equilateral triangular air holes with a side length of $s = 0.3125 \times \sqrt{3}a_0$ and a lattice constant of $\sqrt{3}a_0 = 800$ nm. Perfectly matched layers above and to the transverse (x) sides of the simulation domain provide us with an estimate for the total loss and associated linewidth of the (quasinormal) eigenmodes, defined as two times the imaginary part of the complex eigenfrequency. We also perform simulations in which the transverse perfectly matched layers are replaced by perfect electric-conducting boundaries to eliminate in-plane loss and thus separately quantify the in-plane and out-of-plane (radiative) contributions to the total loss through comparison. We extract the displayed near-field profiles on a regular grid in a plane located 20 nm above the slab.

Device fabrication

The PhC slab was fabricated on a silicon-on-insulator platform with a 220-nm-thick silicon layer on a 3 μm buried oxide layer. First, a positive electron-beam resist with a thickness of 240 nm (AR-P 6200.09) was spin coated. Then, the PhC design was patterned in the resist using electron-beam lithography (Raith Voyager) with 50 kV beam exposure. The electron-beam resist was developed in pentyl acetate/*o*-xylene/methyl isobutyl ketone:isopropanol (9:1)/isopropanol, and the chip subsequently underwent reactive ion etching in HBr and O_2. Finally, the buried oxide layer was removed in an aqueous 4:1 solution of hydrofluoric acid for 19 min and the sample was then subjected to critical-point drying to obtain free-standing PhC membranes[37]. The PhC lattice design features a honeycomb configuration of equilateral triangles (side length, $s = 0.3125a$) in a hexagonal unit cell with lattice constant $a = 827$ nm. The unit-cell shrinking factor was chosen as $\rho = r/r_0 = 0.98$, unless stated otherwise, where r is the distance of the centroids of the triangular air holes from the unit-cell centre; $r = r_0$ for a perfect honeycomb lattice.

Experimental setup

Extended Data Fig. 1 shows a schematic of the optical setup. To measure the photonic dispersion, we use a 200 mW supercontinuum source (SCS; Fianium WhiteLase Micro) that generates light with a broadband spectrum. Its output is filtered by a long-pass filter with a cutoff wavelength of 1,150 nm and coupled into a single-mode optical fibre. Infrared light from the fibre is collimated by an achromatic lens (COL) and passed through a linear polarizer and an achromatic quarter-wave plate, which together define the polarization of the input beam (PO1). A non-polarizing beamsplitter cube (BS) steers the input light to an aspheric microscope objective (MO; Olympus LCPLN50XIR, ×50; numerical aperture, 0.65), which focuses the incident Gaussian beam onto the sample. To precisely position the sample in the focal plane, it is attached to an *XYZ*-movable piezo-actuator (MCL Nano-3D200FT, controlled via MCL ND3-USB163), which itself is mounted atop a manual *XYZ* translation stage for coarse alignment. Reflected light is collected by the same objective and passed through the BS and a second set of linear polarizer and quarter-wave-plate (PO2) to project the back focal plane (BFP) radiation onto the desired polarization state. It then passes a Fourier lens (FL) that, together with a tube lens (TL), images the objective's BFP onto the entrance slit of a spectrometer (Acton SpectraPro SP-2300i). Optional custom spatial filters (SFs) are placed in the image plane between the FL and TL to define the sample area from which light is collected as well as to suppress stray light. The (vertical) entrance slit of the spectrometer is aligned with the optical axis and a cross-cut is selected along $k_x = 0$ in the reciprocal plane, confirmed using a test grating sample. With the help of two parabolic mirrors (PMs) for focusing and collection, the spectrometer grating then disperses the broadband infrared light orthogonally to the slit, such that the InGaAs infrared camera (AVT Goldeye G-008 SWIR) placed at the spectrometer output records images of frequency versus k_y/k_0, where k_0 is the free-space wavevector. The wavevector resolution is $\delta k_y/k_0 \approx 0.009$, and the typical minimal spectral resolution is ~16 GHz.

Extraction of resonance frequencies and quality factors

To extract the centre-mode frequencies and quality factors from the reflection spectra, we fit a set of general (Fano) resonance lineshapes of the form

$$R(\omega) = \left| A_0 + \sum_{j=1}^{n} A_j e^{i\phi_j} \frac{\gamma_j}{\omega - \omega_{0_j} + i\gamma_j} \right|^2, \qquad (5)$$

where A_0 is a constant background amplitude; and A_j, ϕ_j and $\omega_{0_j} - i\gamma_j$ are the amplitude, phase and complex frequency of $n = 2$ individual Lorentzians, respectively. One of these Lorentzians models the PhC mode, whereas the second (broad) Lorentzian accounts for the slowly varying background reflection. Quality factors are defined as $Q_j = \omega_{0_j}/(2\gamma_j)$.

Data availability

The data in this study are available via Zenodo at https://doi.org/10.5281/zenodo.10125585.

References

44. COMSOL Multiphysics version 5.2. *COMSOL AB* https://www.comsol.com/ (2015).

Acknowledgements

We thank S. Arora and D. Muis for fruitful discussions. This work is part of the research programme of the Netherlands Organisation for Scientific Research (NWO). We acknowledge support from the European Research Council (ERC) Starting Grant no. 759644-TOPP and Advanced Investigator grant no. 340438-CONSTANS.

Author contributions

R.B. and E.V conceived the project. R.B. fabricated the devices, carried out the measurements, performed the data analysis and modelling, and drafted the paper. E.V. and L.K. supervised the project. All authors contributed extensively to the interpretation of the results and writing of the paper.

Competing interests

The authors declare no competing interests.

Additional information

Extended data is available for this paper at https://doi.org/10.1038/s41566-024-01412-3.

Supplementary information The online version contains supplementary material available at https://doi.org/10.1038/s41566-024-01412-3.

Correspondence and requests for materials should be addressed to Ewold Verhagen.

Peer review information *Nature Photonics* thanks the anonymous reviewers for their contribution to the peer review of this work.

Reprints and permissions information is available at www.nature.com/reprints.

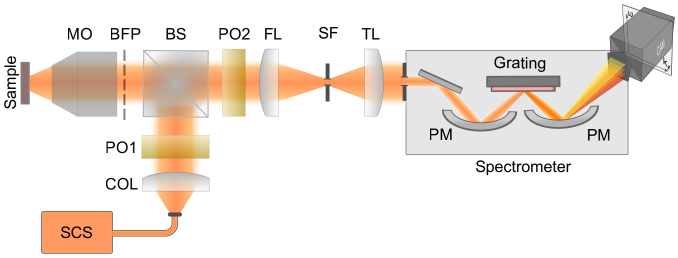

Extended Data Fig. 1 | Far-field Fourier spectroscopy. Schematic depiction of the experimental far-field Fourier spectropolarimetry setup used for angularly resolved measurement of the photonic crystals' band dispersion. See Methods for details and abbreviations.

https://doi.org/10.1038/s41566-024-01412-3

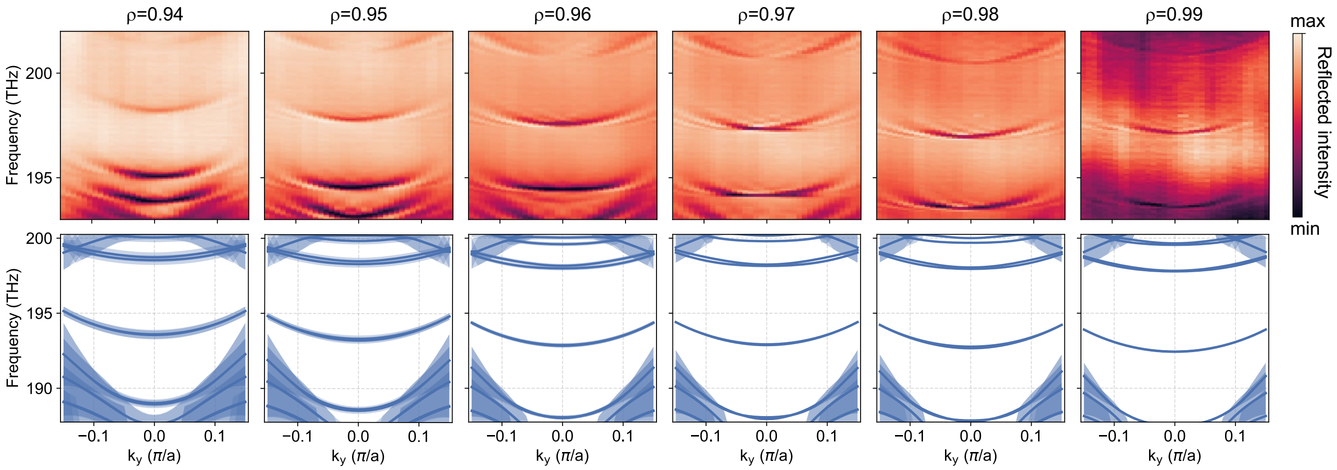

Extended Data Fig. 2 | Symmetry breaking to control radiative coupling. Measured (top) and simulated (bottom) bands of Landau levels in PhCs with varying unit cell shrinking factor ρ, all at $\kappa = 0.125$. The linewidth in the simulations is scaled by a factor two for enhanced visibility. The linewidth increases with decreasing ρ.

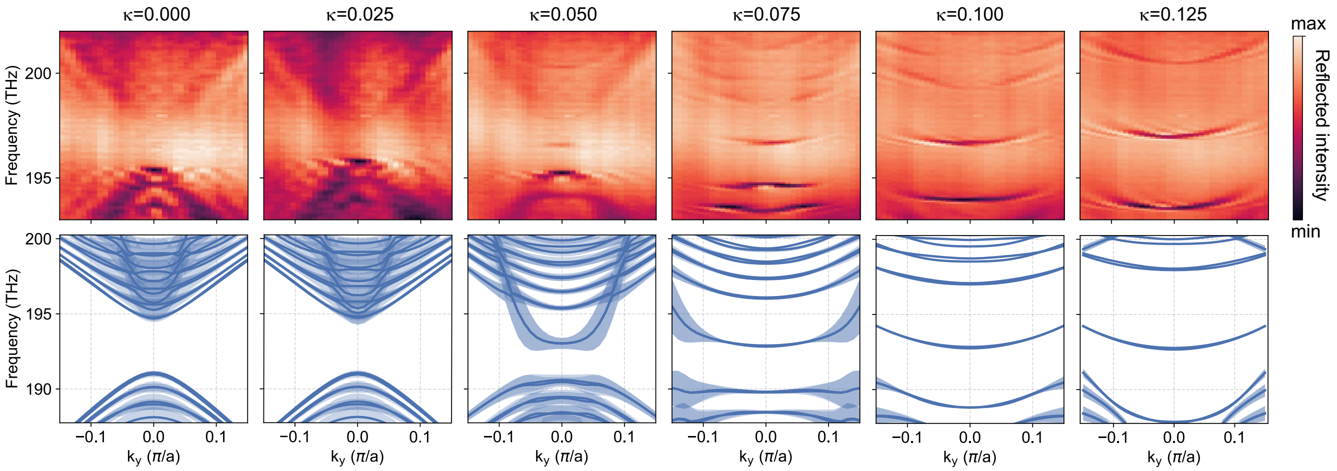

Extended Data Fig. 3 | Tailoring Landau levels via strain. Measured (top) and simulated (bottom) bands of Landau levels in PhCs with increasing strain magnitude κ, all at $\rho = 0.98$. The gap at small κ is due to the sub-lattice symmetry breaking.

https://doi.org/10.1038/s41566-024-01412-3

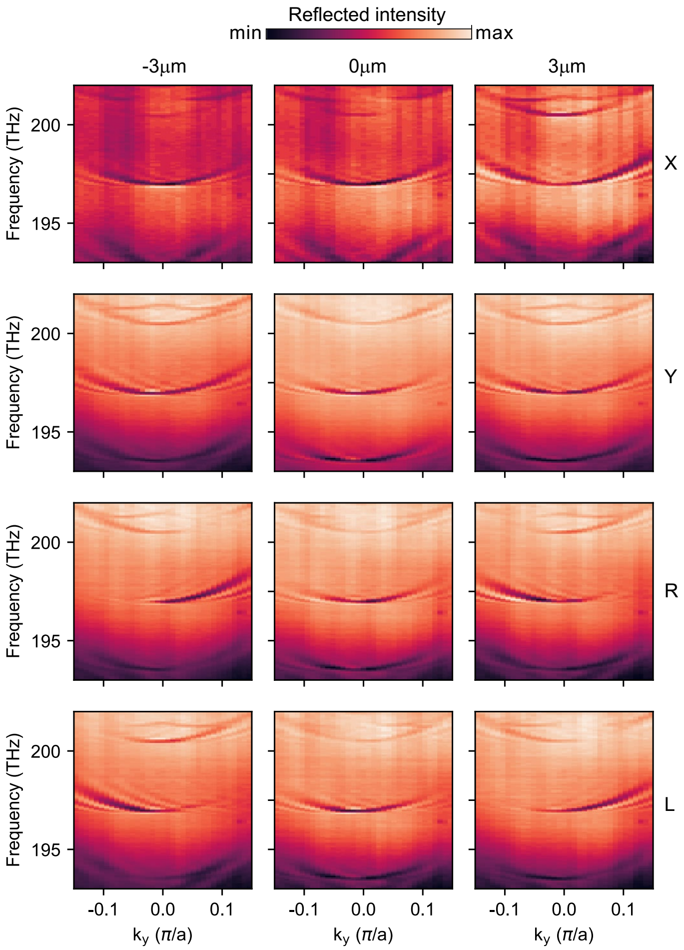

Extended Data Fig. 4 | Landau level localization and polarization. Position- and polarization-dependent excitation of photonic Landau levels, where the displacement in x relative to the lattice center and the polarization state of the incident beam (linear horizontal (X), linear vertical (Y), right-handed circular (R) and left-handed circular (L)) are indicated ($\rho = 0.98$ and $\kappa = 0.125$ in these measurements).

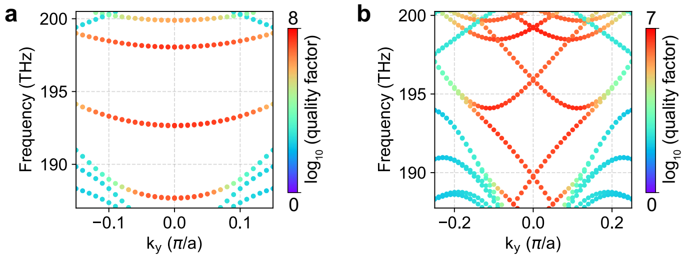

Extended Data Fig. 5 | Quality factors of pristine lattices. a, Numerically retrieved bands of a pristine strained photonic crystal featuring Landau levels, with color-coded quality factors ($\rho = 1.00$, $\kappa = 0.125$). **b**, Same as **a**, for a photonic crystal featuring chiral edge states.

https://doi.org/10.1038/s41566-024-01412-3

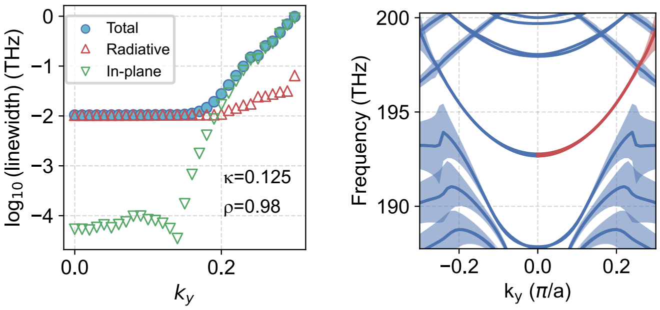

Extended Data Fig. 6 | Landau level losses versus wavevector. Numerically retrieved contributions of radiative and in-plane losses to the total linewidth of the zeroth Landau level (left), corresponding to the section of the band highlighted in red (right). For large k_y, the in-plane losses exceed the radiative losses to the top and bottom of the PhC slab, which reduces the visibility of the bands in the experiment as they become under-coupled to the free-space radiation.

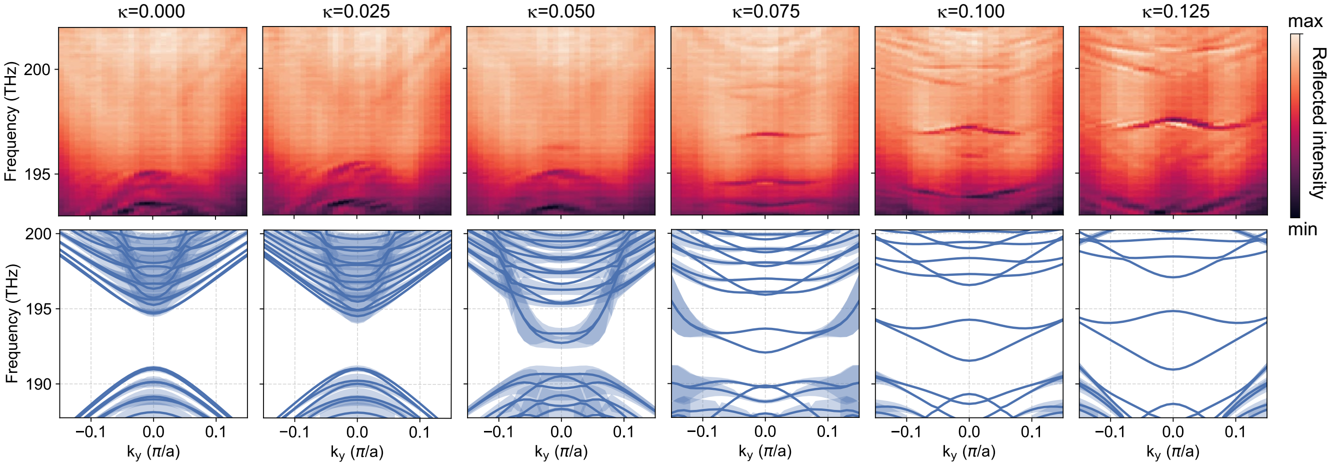

Extended Data Fig. 7 | Tailoring chiral edge states via strain. Measured (top) and simulated (bottom) bands of chiral edge states in PhCs with increasing strain magnitude κ, all at $\rho = 0.98$.

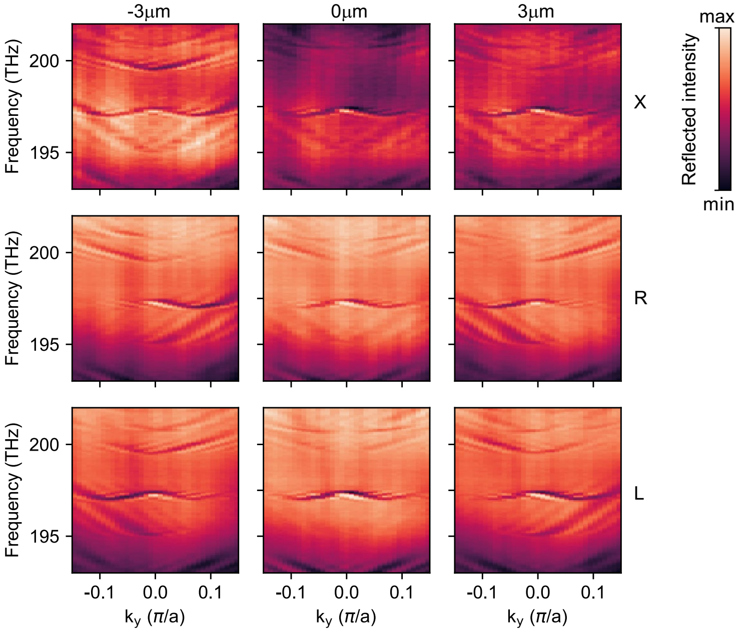

Extended Data Fig. 8 | Polarization and position dependence of chiral edge states. The incident polarization state is denoted as X (linear horizontal), R (right-hand circular), or L (left-hand circular) besides each row. The transverse position of the focus with respect to the interface between the domains is shown above each column. The strain magnitude is $\kappa = 0.125$ for all panels. For right- and left-handed circularly polarized light, we see signatures of spin-orbit coupling in the chiral edge states. At a fixed frequency, one can selectively couple into forward or backward propagating modes by changing the helicity (pseudospin) of the incident beam. However, we note that the same state can be launched with opposite helicity at the other side of the center. Moreover, the panels show that two different edge states can be excited at the same location with equal helicity, despite having opposite group velocity.

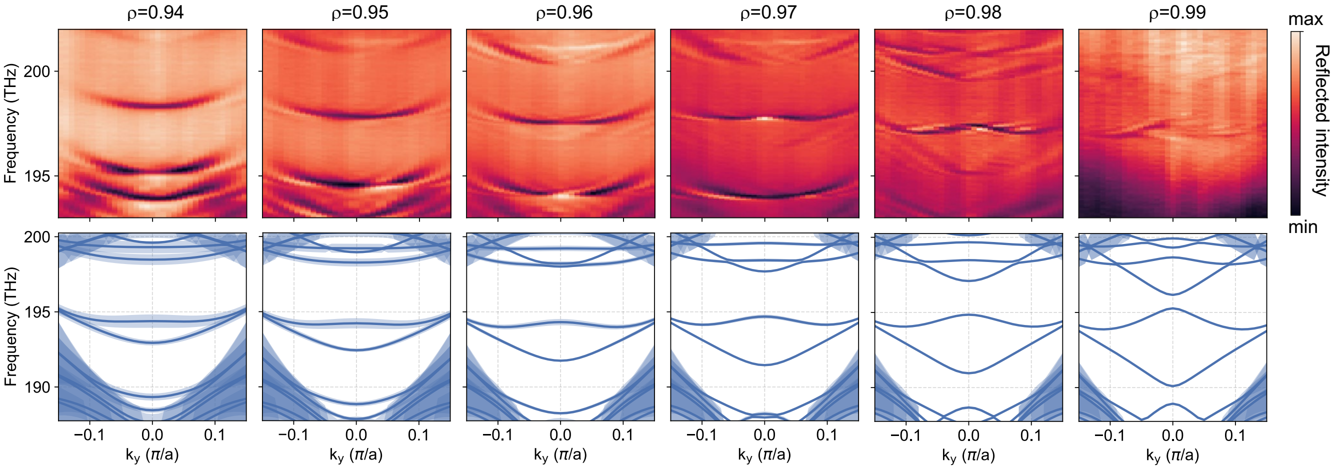

Extended Data Fig. 9 | Sub-lattice symmetry breaking and edge state dispersion. Measured (top) and simulated (bottom) bands of chiral edge states in PhCs with varying unit cell shrinking factor ρ, all at $\kappa = 0.125$. The linewidth is scaled by a factor two for enhanced visibility. The sub-lattice symmetry breaking leads to avoided crossings around the Γ point in the edge state dispersion.